Bonding and Magnetic Trends in the [AnIII(DPA)3]3- Series Compared to the Ln(III) and An(IV) Analogues

Md. Ashraful Islam, Claude Berthon, Julie Jung, Hélène Bolvin

Bonding and magnetic trends in the $[An^{III}(DPA)_3]^{3-}$ series as compared to the Ln(III) and An(IV) analogs.

Md. Ashraful Islam[†¶*], Claude Berthon[‡], Julie Jung[§], Hélène Bolvin[†*]

[†] Laboratoire de Chimie et Physique Quantiques, CNRS, Université Toulouse III, 118 route de Narbonne, 31062 Toulouse, France.
[‡] CEA, DES, ISEC, DMRC, Univ Montpellier, Marcoule, France.
[§] Theoretical division, Los Alamos National Laboratory, Los Alamos, New Mexico 87545, USA.
[¶] Present address: Centre de Résonance Magnétique Nucléaire à Trés Hauts Champs - CRMN, 5 Rue de la Doua, 69100 Villeurbanne, France.
[*] e-mail addresses: aislam@irsamc.ups-tlse.fr; bolvin@irsamc.ups-tlse.fr

Abstract

The crystal field parameters are calculated from first principles in the $[An^{III}(DPA)_3]^{3-}$ series, completing previous work on the $[Ln^{III}(DPA)_3]^{3-}$ and $[An^{IV}(DPA)_3]^{2-}$ series. The crystal field strength parameter follows the Ln(III) < An(III) < An(IV) trend. The parameters deduced at the orbital level decreases along the series while the J-mixing impacts strongly the many-electron parameters, specially for the Pu(III) complex. We further compile the available data for the three series. In some aspects, the An(III) are closer to the Ln(III) than to the An(IV) complexes, as for the geometrical structure and the bonding descriptors. At the beginning of the series, up to Pu(III), there is quantitative departure from the free ion, specially for the Pa(III) complex. The magnetic properties of the actinides keep the trends of the lanthanides, in particular the axial magnetic susceptibility follows qualitatively Bleaney theory.

Introduction

Actinide chemistry remains a major field of research since the actinides offer a rich chemistry, close to the transition metals due to the resemblance of the metal ligand interaction to those of *d* orbitals interactions[1–3] as well as they exhibit the same potentiality as the lanthanides in terms of promising magnetic properties.[4,5] It is informative to analyze the trends by following an indicator through the series; it can be Gibbs free energy of complexation,[6] determined both experimentally and from DFT calculations, bond order analysis, the energy and the composition of the orbitals from first principles calculations, energy decomposition[6–10] and finally the crystal-field parameters (CFPs). The whole $[An^{III}Cl_6]^{3-}$ series has been studied both experimentally[11] and theoretically.[12–14] Concerning the $[An^{III}(DPA)_3]^{3-}$ (DPA = dipicolinate) series, there are few experimental data for the beginning of the series, because An(III) spontaneously evolves to different oxidation states (from An(IV) to An(VI)). The middle of the series is the best documented. XRD structures of $[An(DPA)_3(C_3H_5N_2)_3]\cdot 3H_2O$ for An = Pu and Am[15] and $[An^{III}(HDPA)_3]\cdot nH_2O$ for An = Am, Cm, Bk and Cf[16,17] were determined. The Pu(III), Am(III), Cm(III) and Cf(III) complexes were characterized by paramagnetic NMR, the Am(III) one using EXAFS, and the Bk(III) and Cf(III) complexes by absorption and magnetometry spectroscopies and the complexation of the Am-Cf species analyzed by thermodynamic measurements.[6] The late actinides, after berkelium, do not possess long-life isotopes to allow the recording of experimental data. The bonding in the $[An^{III}(DPA)_3]^{3-}$ series has been recently described using DFT and CAS based methods[6,10] methods. The $[Ln^{III}(DPA)_3]^{3-}$ and $[An^{IV}(DPA)_3]^{2-}$ series are well characterized as well, by XRD and NMR spectroscopies[15,18–21] and first-principles CFPs.[22,23] All of this put together results in a data set that allows for detailed comparative analysis of the three series.

In this work, we calculate the CFPs in the $[An^{III}(DPA)_3]^{3-}$ series from first principles. In last few decades, CAS based methods have shown their capability to describe the excited states and magnetic properties of metallic complexes with open shell *f* orbitals. CAS approaches are successful in rationalizing the electronic spectra and magnetic properties. Observed macroscopic properties such as magnetic susceptibility of the actinide complexes are reportedly well reproduced from the molecular calculations as well as the spectral properties.[24]

The CFPs are based on the century old crystal-field theory which is based on a model Hamiltonian that describes the electrostatic interaction of the free ion with the ligand environment. The parameters are usually determined as phenomenological parameters from experimental data. One can still feel the flavor of the *LS* (or Russell-Saunders) coupling scheme, at the least for the low lying states, and this allows a determination of the CFPs from first principles. The CFPs in the $[An^{III}(DPA)_3]^{3-}$ series are further compared to the $[Ln^{III}(DPA)_3]^{3-}$ and $[An^{IV}(DPA)_3]^{2-}$ analogs. This is further completed by the comparison of the structural parameters, QTAIM indicators and magnetic properties in the three series, leading to a comprehensive analysis of the trends in the three series.

Computational details

geometry optimization The geometry of the complexes were optimized with ORCA 4.2.1[25] within the density functional theory (DFT) framework using the GGA BP86 functional[26] with the D3BJ dispersion correction[27] and TightSCF and TightOpt convergence options for the highest spin state. DKH-def2-TZVPP basis sets are used for oxygen, carbon, nitrogen and hydrogen; SARC-DKH-TZVPP[28] basis sets are used for the metal center. Def2/JK auxiliary basis sets are used for oxygen, carbon, nitrogen and hydrogen atoms and the autoaux feature[29] is used to generate the auxiliary basis for the metal centers. The RI-JK approach is used for the resolution of the identity.[30]

electronic structure Wave-function based calculations have been performed on both the extrapolated (see Section S1Geometry of the complexessection.1) and DFT optimized structures. The AILFT calculations are performed using ORCA 4.2.1[25] with the same basis sets as geometry optimizations. Scalar relativistic effects are account for using the DKH2 Hamiltonian.[31,32] Quasi-degenerate perturbation theory is used to account for spin-orbit coupling.[33] In the CASSCF and NEVPT2 calculations,[34–36] the active space is composed of the seven $5f$ orbitals of the An and associated N electrons i.e. CAS(N,7). For each element, we compute all the roots of all the spin states this active space leads to. The ITO CFPs were calculated using MOLCAS 7.8.[37] Firstly, a state-averaged SF-CASSCF (spin-free complete active space self consistent field)[38] calculations were performed with same active space as defined above. Dynamic correlation was added using the SS-CASPT2 (state-specific complete active space perturbation theory at 2nd order)[39] method with a level shift of 0.5 a.u. (except for Pa, 0.8 a.u.) in state specific manner i.e. state by state on top of CASSCF wave functions. Relativistically contracted cc-pVTZ-DK3[40,41] basis with TZP quality for the An, and the ANO-RCC[42] with TZP quality for O, N, DZP for C and DZ for H atoms. Douglas-Kroll-Hess transformed Hamiltonian at the 3rd order i.e. DKH3 was used to treat the relativistic effects both scalar (SF) and spin-orbit (SO).[43,44] Spin-orbit coupling was calculated as state interaction between the SF-CASSCF states with the RASSI (restricted active space state interaction) module,[45] and using the CASSCF and dynamic correlation corrected SS-CASPT2 energies leading to the SO-CASSCF and SO-CASPT2 results, respectively. All the roots of the maximum spin (S) multiplets were undertaken for the computation of the spin-orbit coupling matrices, for the $S-1$ multiplets: 28 for Pa and Md, 43 for U and Fm, 99 for Np and Es, 128 for Pu and Cf, 91 for Bk were considered, and for the $S-2$ multiplets: 31 for Np and Es, 98 for Pu and Cf, 91 for Bk were considered. SO integrals were calculated using the AMFI (atomic mean-field integrals) approximation.[46] CFPs were calculated with a local program written in Mathematica as described in ref.[22] Magnetic g factors were calculated according to ref.[47]

Results and discussions

The $[An^{III}(DPA)_3]^{3-}$ series is isostructural to the $[Ln^{III}(DPA)_3]^{3-}$ and $[An^{IV}(DPA)_3]^{2-}$ series.[15,23] The metal is coordinated by three DPA ligands forming a tricapped trigonal distorted prism (see Figure 1). Each ligand is tridentate, and coordinated to the cation through the nitrogen atom of the pyridine cycle (capped position), and the two oxygen atoms of the carboxylate groups (prism position). XRD structures of $[An(DPA)_3(C_3H_5N_2)_3]\cdot 3H_2O$ for An = Pu and Am[15] and $[An^{III}(HDPA)_3]\cdot nH_2O$ for An = Am, Cm, Bk and Cf[16,17] were determined. The structures of $[Am(DPA)_3(C_3H_5N_2)_3]\cdot 3H_2O$ and $[Am^{III}(HDPA)_3]\cdot nH_2O$ are very similar, showing that the protonation of the DPA^{2-} ligand does not impact the bonding scheme of the central cation. Figure 2 compares the metal-ligand distances, for the available XRD and DFT optimized structures. For the XRD structures, the M-L distance follows a decrease along the series, in accordance with the decrease of the ionic radii. It has been shown that in some actinide series, the metal-ligand distance shows some 'breaks' between Pu and Am and then between Bk and Cm, in the sense that the decrease in the bond length is larger than expected.[14,48] It is apparently not the case in the present series. The trend for the M-L distance from DFT optimized structures using the GGA functional BP86 is really erratic. The structures optimized by Yu *et al.* using the hybrid functional PBE0 were published after we started this work; the trend is more regular, but still

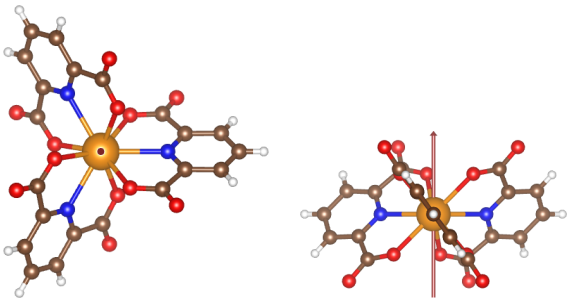

Figure 1: $[An^{III}(DPA)_3]^{3-}$ complexes, top view (left) and side (right) views. Color code: orange-Np, blue- N, red- O, saddle-brown- C, white- H. The C_3 axis (denoted z axis) is shown in light red color.

do not match perfectly the experimental trends.[14] The ionic bond lengths determined as the sum of the ionic radius of the nine-coordinate An ion[49] of the O and N ions by Shannon[50] are larger than the XRD bond lengths.

In Figure 3a, the distances in the coordination sphere for the available crystallographic structures of the $[Ln^{III}(DPA)_3]^{3-}$, $[An^{III}(DPA)_3]^{3-}$ and $[An^{IV}(DPA)_3]^{2-}$ series are represented in terms of the ionic radius of the nine-coordinate central metal, as determined by d'Angelo et al[51] for the Ln(III) and by David et al[49] for the An(III) and An(IV). The trends are linear, with a slope smaller than one. The curves are very similar for the Ln(III) and An(III) cations, suggesting that the covalent effects do not impact so much the bonding distances. On the contrary, the trends for the An(IV) cations are different. While the An(IV)-O distances are the same as for An(III) and Ln(III), the An(IV)-N distances are longer (≈ 0.1 Å). There is a deformation of the DPA ligand in order to 'keep' the optimal bonding distances for the O and N atoms., as shown for the internal ONO angle in Figure 3c: the biting angle denotes a linear trend with the ionic radii for the three series, and as a consequence of the larger An(IV)-N distances, it is much smaller in the An(IV) series.

The CFPs are very sensitive to geometrical structure. Since our DFT optimized structures do not confirm the experimentally observed trend, we built the structures of the whole $[An^{III}(DPA)_3]^{3-}$ series by extrapolating the two crystallographic structures for the Pu(III) and Am(III) derivatives, as described in Section S1Geometry of the complexessection.1 of the SI (see Figure 2). We consider both the extrapolated and DFT optimized series to compute the electronic structures. But if not mentioned specifically, the reported energy levels, analysis of wave function and the trends of the CFPs are based on the extrapolated geometric structures.

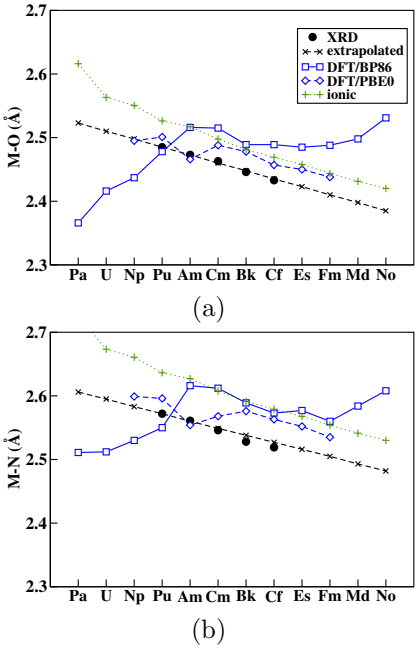

Figure 2: An-O (a) and An-N (b) bond distances (in Å) along the $[An^{III}(DPA)_3]^{3-}$ series of the experimental (circles), extrapolated (crosses), DFT optimized (squares and diamond[14]) and ionic (plus) structures. The ionic bond lengths ($r_{An^{3+}} + r_{O^{2-}/N^{3-}}$) are determined from the ionic radii.

CAS based energy levels

The energy levels of the $[An^{III}(DPA)_3]^{3-}$ complexes are given in Tables S4SF energy levels (in cm^{-1}) from CASSCF and CASPT2 methods in MOLCAS. S stands for the states with the highest spin multiplicity and $S-1$ for the excited reduced spin states. Ground L manifolds are separated by horizontal lines.table.caption.6 and S5SF energy levels (in cm^{-1}) from CASSCF and NEVPT2 methods in ORCA. S stands for the states with the highest spin multiplicity and $S-1$ for the excited reduced spin states. Ground L manifolds are separated by horizontal lines.table.caption.8 before spin-orbit coupling (SF), and in Tables S6SO energy levels (in cm^{-1}) from CASSCF and CASPT2 methods in MOLCAS. Ground J manifolds are separated by horizontal lines.table.caption.10 and S7SO energy levels (in cm^{-1}) from CASSCF and NEVPT2 methods in ORCA. Ground J manifolds are separated by horizontal lines.table.caption.12 with spin-orbit coupling. The ab initio energy levels of the ground J manifolds are plotted in Fig. S2Energy spans of the ground J manifolds (in cm^{-1}) of the $[An^{III}(DPA)_3]^{3-}$ complexes calculated with ORCA (a) and MOLCAS (b). Horizontal lines : SO-CASSCF, dots : SO-NEVPT2/SO-CASPT2.figure.caption.14. The SO-CASSCF energies (showed by horizontal lines in Fig. S2Energy spans of the ground J manifolds (in cm^{-1}) of the $[An^{III}(DPA)_3]^{3-}$ complexes calculated with ORCA (a) and MOLCAS (b). Horizon-

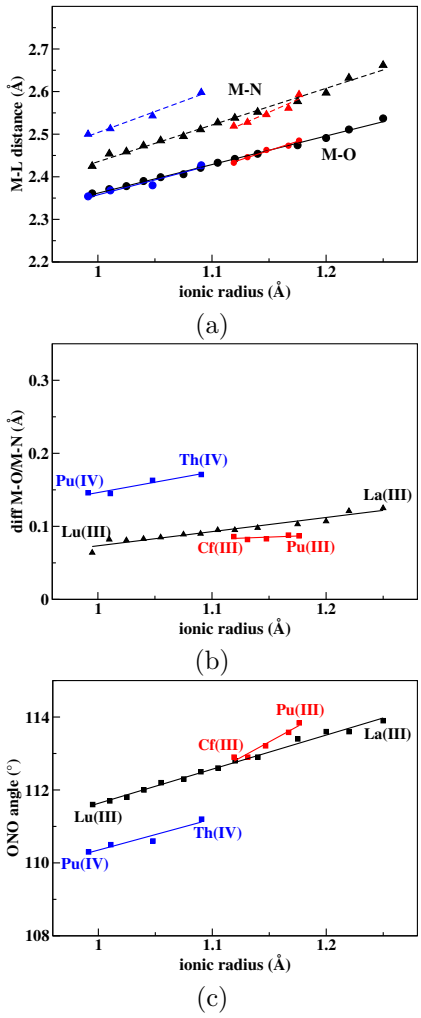

Figure 3: M-O (circles) and M-N (triangles) bond distances (a, in Å), their difference (b, in Å) and the O-N-O angle (c, in °) from the XRD structures along the $[Ln^{III}(DPA)_3]^{3-}$ (black), $[An^{III}(DPA)_3]^{3-}$ (red) and $[An^{IV}(DPA)_3]^{2-}$ (blue) series as a function of the ionic radii.

tal lines : SO-CASSCF, dots : SO-NEVPT2/SO-CASPT2.figure.caption.14) calculated with MOLCAS (Fig. S2Energy spans of the ground J manifolds (in cm^{-1}) of the $[An^{III}(DPA)_3]^{3-}$ complexes calculated with ORCA (a) and MOLCAS (b). Horizontal lines : SO-CASSCF, dots : SO-NEVPT2/SO-CASPT2.figure.caption.14a) and ORCA (Fig. S2Energy spans of the ground J manifolds (in cm^{-1}) of the $[An^{III}(DPA)_3]^{3-}$ complexes calculated with ORCA (a) and MOLCAS (b). Horizontal lines : SO-CASSCF, dots : SO-NEVPT2/SO-CASPT2.figure.caption.14b) are similar, but differ with the inclusion of dynamic correlation with either CASPT2 or NEVPT2 (denoted by the dots). This is expected since the two methods differ by the definition of the zeroth order and the perturbed Hamiltonian. The energy splitting of the ground J manifold ranges from as low as 200 cm^{-1} for the Pu(III) complex to 1500 cm^{-1} for the Pa(III) one. The span of a ground J manifold is larger with the NEVPT2 than CASPT2 method. The ground doublet of the Kramers ions (U, Pu, Cf, Fm and No) are quite similar with all methods, as shown by the values of the g-factors shown in Table S8g_1, g_2, g_z (g_z is assigned the to g factor which makes the smallest angle with the pseudo C_3 axis) of the ground Kramers doublets from different methods of calculations.table.caption.16.

Degree of J-mixing

In the free ion, the ground $^{2S+1}L_J$ term defined in the Russell-Saunders coupling scheme couples by spin-orbit coupling with excited terms with the same value of J: this is the so-called intermediate coupling scheme, or J-mixing. Since the spin-orbit coupling is calculated as a state interaction, it is possible to quantify this mixing as given in Table 1. Furthermore, it allows to evaluate the CFPs from the LS wave functions. In the $[An^{III}(DPA)_3]^{3-}$ complexes, the contributions of the ground ^{2S+1}L manifold to the ground J manifold ranges from 75 to 97%. This is of the same order as for the free ion and for the $[An^{III}Cl_6]^{3-}$ complexes,[13] and quite smaller than for the lanthanide series where this contribution is close to 98%. In all cases, the most contributing excited state corresponds to $\Delta L = \pm 1$ and $\Delta S = \pm 1$ with the ground state allowing the same value of J and first-order spin-orbit coupling. In the free-ion, only J-mixing is allowed by the spherical symmetry. The weight are very similar in the complexes, denoting that the J-mixing remains the main spin-orbit effect. The energy gap with this excited manifold is plotted in Figure S3SF-CASPT2 energy (in cm^{-1}) of the excited $^{2S'-1}L'$ manifold contributing the most to the ground J manifold in the $[An^{III}(DPA)_3]^{3-}$ complexes.figure.caption.15. The large J-mixing in the actinides in comparison to the lanthanides is a result of i) an increased spin-orbit

Table 1: Weight of the principal ^{2S+1}L terms in the ground J manifold for the free An^{3+} ions, the $[An^{III}Cl_6]^{3-}$ (from[10]) and $[An^{III}(DPA)_3]^{3-}$ complexes from SO-CASSCF calculations with MOLCAS.

An	Free Ion	$[An^{III}Cl_6]^{3-}$	$[An^{III}(DPA)_3]^{3-}$
Pa	92% ^3H + 8% ^1G		90% ^3H + 7% ^1G
U	89% ^4I + 10% ^2H	85% ^4I + 7% ^2H	89% ^4I + 10% ^2H
Np	88% ^5I + 11% ^3H	87% ^5I + 11% ^3H	88% ^5I + 8% ^3H
Pu	80% ^6H + 15% ^4G	78% ^6H + 12% ^4G	79% ^6H + 7% ^4G
Bk	82% ^7F + 14% ^5G	79% ^7F + 12% ^5G	82% ^7F + 12% ^5G
Cf	76% ^6H + 20% ^4I	75% ^6H + 15% ^4I	77% ^6H + 9% ^4I
Es	79% ^5I + 19% ^3J	77% ^5I + 16% ^3J	79% ^5I + 19% ^3J
Fm	92% ^4I + 8% ^2J		91% ^4I + 8% ^2J
Md	98% ^3H + 2% ^1I		97% ^3H + 3% ^1I

coupling ii) a decrease of $5f$ electron-electron interaction due to the larger radial extension of the $5f$ orbitals. One can notice from Table 1 that the J-mixing is specially important in the middle of the actinide series for Pu, Cf and Es.

Trends of the Slater-Condon and spin-orbit parameters

The AILFT parameters are deduced from the entire ab initio energy spectrum within the $5f^N$ configuration (see Section S2.2ITO and AILFT methodssubsection.2.2 for more details). The rotation $\mathscr{C}_3$ axis is taken as the z axis. The spectrum is fitted by the 27 CFPs B_q^k, the three Slater-Condon parameters F^2, F^4 and F^6 which model the many-electron interaction and the one-electron effective spin-orbit parameter ξ. Thus, the AILFT method describes explicitly the many-electron interaction. The AILFT parameters are tabulated in Table S12Slater–Condon (F^2, F^4 and F^6), SOC (ζ) parameters (in cm^{-1}) and nephelauxetic reduction factor α (in %) calculated with AILFT method for the $[An^{III}(DPA)_3]^{3-}$series. The free ion parameters are collected from Ref.[7] table.caption.21 and plotted in Figure 4 and compared to the free ion[13] and $[Ln^{III}(DPA)_3]^{3-}$ complexes.[22] This method is based on a one-to-one correspondence of the ab initio active orbitals with the $5f$ orbitals. Table S9Weight (in %) of the actinide atomic $5f$ orbitals in the CASSCF active orbitals with ORCA. Deviation from 100% represents the mixing of the actinide $5f$ orbitals with other type of orbitals.table.caption.17 gives the contribution of the $5f$ orbitals to the seven active CASSCF orbitals. In the beginning of the series, the $5f$ orbitals are significantly mixed with other orbitals especially for Pa, but in the second-half, the active orbitals are almost purely $5f$. At the beginning of the series, the energy gap in between the actinide valence $5f$, $6d$ and $7s$ subshells is smaller and the bonding with the ligands is mediated by a significant participation of these valence orbitals. Further in the series, the $5f$ orbitals become more inner core limiting their admixture with the $6d$ and $7s$ shells.

The Mulliken atomic spin population analysis of the SF-CASSCF ground state in Table S10Mulliken spin population in the SF-CASSCF ground state of the extrapolated and DFT optimized structures with MOLCAS. ρ^s is the total atomic spin on the actinide center and ρ^s_{5f}, ρ^s_{6d} are its components in the actinide $5f$ and $6d$ orbitals, respectively. $1-\frac{\rho^s}{N}$ represents the degree of spin delocalization from the actinide to the ligands, N is the number of $5f$ electrons. table.caption.18 and Figure S4Mulliken spin population in the atomic $6d$ orbitals and metal-to-ligand spin delocalization for the SF-CASSCF ground state with MOLCAS of the $[An^{III}(DPA)_3]^{3-}$ series. Solid and dotted lines represent the values for the extrapolated and DFT optimized structures, respectively.figure.caption.19 shows a significant spin population in the atomic $6d$ orbitals up to Bk, and much larger in the case of Pa due to the significant energy overlap of the $5f$-$6d$ subshells for the latter. The metal-to-ligand Mulliken spin delocalization in the ground state shown in Fig. S4Mulliken spin population in the atomic $6d$ orbitals and metal-to-ligand spin delocalization for the SF-CASSCF ground state with MOLCAS of the $[An^{III}(DPA)_3]^{3-}$ series. Solid and dotted lines represent the values for the extrapolated and DFT optimized structures, respectively.figure.caption.19 gradually decreases in the first half of the series and again slightly increases at the second half. The valence 6d and 7s subshells are primarily involved in bonding interactions through orbital overlap. As already mentioned, the mixing between those orbitals decreases due to the increase of the 5f to 6d energy gap and consequently, the delocalization of the spin density on the ligands. At the end of the series, the 5f orbitals approach the ligand orbitals energetically, favoring again the delocalization of the spin density.

The three Slater-Condon parameters (see Figure 4 and Table S12Slater–Condon (F^2, F^4 and F^6), SOC (ζ) parameters (in cm^{-1}) and nephelauxetic reduction factor α (in %) calculated with AILFT method for the $[An^{III}(DPA)_3]^{3-}$series. The free ion parameters are collected from Ref.[7] table.caption.21) are close to the values for the free ion,[13] except at the beginning of the series. They increase along the series due to the increase of the $5f$ electron numbers and the contraction of the $5f$ orbitals. They are greatly reduced compared to the lanthanides, due to the larger radial extension of the $5f$ orbitals. In the central Coulomb field approximation, the ratios of F^4/F^2 and F^6/F^2 for trivalent lanthanide ions are very close to 0.70 and 0.54, respectively.[52,53] This ratios are kept for the trivalent actinide ions, except for the Pa(III) complex, which is the most deviated case from the free ion, as mentioned pre-

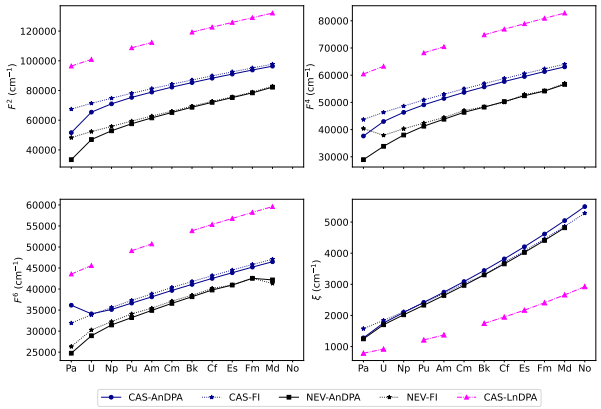

Figure 4: Slater-Condon parameters F^2, F^4 and F^6 and the spin-orbit parameter ζ for the An(III) free ions (dotted, from[13]) and the $[An^{III}(DPA)_3]^{3-}$ (plain) series (CASSCF: blue, NEVPT2: black) and the $[Ln^{III}(DPA)_3]^{3-}$ (CASSCF, magenta, from[22]) series.

viously. As expected, accounting for electron dynamic correlation greatly reduces the magnitude of the three Slater-Condon parameters (compare CASSCF and NEVPT2 values). From Am to the end of the series, the parameters are slightly lower than for the free ion. The nephelauxetic reduction factor $\alpha = 1 - \frac{p^{complex}}{p^{FI}}$ where $p^{complex}$ and p^{FI} are the values of the parameters in the complex and free ion, respectively, expresses the deviation from the free ion, due to the electron-cloud expansion over the ligands. Up to Pu, they pull apart from the free ion values, the nephelauxetic reduction lies between 4% (in Pu) to 22% (in Pa). The nephelauxetic reduction beyond Pu is less than 2% as observed in the $[Ln^{III}(DPA)_3]^{3-}$ series.[22] This shows that the late actinides are closer to the free ions. The spin-orbit parameter ζ increases along the series due to the increase of the effective nuclear charge and the decrease of the radial extension of the $5f$orbitals. Overall, the value for ζ in the $[An^{III}(DPA)_3]^{3-}$ complexes are close to the corresponding free ion values indicating a quite small mixing with the ligand orbitals. ζ is not so much affected by the dynamic correlation unlike the Slater-Condon parameters, as the dynamic correlation is a two-electron phenomenon.

ITO vs AILFT crystal field parameters

Two methods are proposed to extract the CFPs from first principles CAS calculations as summarized in Section S2.2ITO and AILFT methodssubsection.2.2; a) the AILFT (Ab Initio Ligand Field Theory) method[54,55] developed by Atanasov and Neese is a least square fit technique and extracts the CFPs from the whole ab initio f configuration energy spectrum, b) the ITO (Irreducible Tensor Operator) method[56] suggested by Ungur and Chibotaru is a tensor decomposition technique where the CFPs are extracted from the Hamiltonian matrix of the ground L (without spin-orbit) or J (with spin-orbit) manifolds. With the ITO technique, the CFPs take into account effectively the two-electron effects and the spin-orbit effects, if applicable. The parameters of 6th orders are not deducible for manifolds with $J < 3$ and it is not possible to evaluate the ITO-CFPs for Am with spin-orbit (with $J = 0$) and for the spin-only Cm case. The quality of the ITO technique is probed by the distance between the ab initio and model matrices for the moment and the energy (see Eqs. S8ITO and AILFT methodsequation.2.8 and S9ITO and AILFT methodsequation.2.9 and Table S13δL_u ($u = x,y,z$) (in μ_B), δm_u ($u = x,y,z$) (in μ_B) and δh (in cm^{-1}) distances between *ab initio* and model matrices (see Eqs. S8ITO and AILFT methodsequation.2.8 and S9ITO and AILFT methodsequation.2.9).table.caption.22). The values are larger than the corresponding Ln(III) complexes[22] and smaller than the corresponding An(IV) complexes.[23] In all cases, the distances between ab initio and model matrices are small, and this attests the availability of this technique to quantify the CFPs in the $[An^{III}(DPA)_3]^{3-}$ series. In the second half of the series, the distances are small, indicating that the wave functions in the complexes are close to those of the free ion. When the dynamical correlation is included, δh increases when $J > 3$, which shows that terms of order more than 6 should be introduced, but the effects is still negligible. It is at the very beginning of the series, specially for Pa that the differences between the ab initio and the model spaces are the largest.

The ITO-CFPs and AILFT-CFPs are tabulated in Tables S14ITO CFPs (in cm^{-1}) from SF-CASSCF, SO-CASSCF and SO-CASPT2 methods. table.caption.23 and S15AILFT CFPs (in cm^{-1}) from SO-CASSCF and SO-NEVPT2 methods. table.caption.24. Indeed the six CFPs B_0^2, B_0^4, B_0^6, B_3^4, B_3^6 and B_6^6 are dominant according to the trigonal spatial symmetry of the coordination environment. Some of the parameters related to rhombic and triclinic symmetry ($\bar{B}_1^2$, $\bar{B}_2^2$, $\bar{B}_1^4$, $\bar{B}_2^4$) are found non negligible (i.e. > 100 cm^{-1}) but they are several orders of magnitude smaller than the dominant ones, except for Pa. The three axial AILFT CFPs B_0^2, B_0^4, B_0^6 (represented in Fig. S5The three axial CFPs B_0^2, B_0^4 and B_0^6 along the $[An^{III}(DPA)_3]^{3-}$ series.figure.caption.25) are rather constant along the series whereas their variation is more erratic at the beginning of the series in the case of ITO.

The crystal field total strength parameter S includes the combined effects of the 27 CFPs into a single parameter as defined by Eq. S6Theoryequation.2.6. This parameter is rotational invariant, it means independent of the Cartesian frame, while the CFPs are. Its is a very convenient tool for comparing series by reducing the discussion to only one

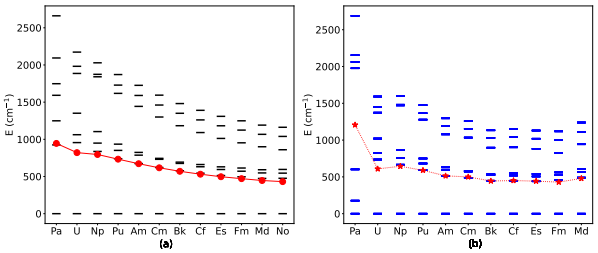

Figure 5: Energy span of the $5f$ (black, in cm^{-1}) and crystal-field strength parameter S (red, in cm^{-1}) from CASSCF (a) and NEVPT2 (b) in the $[An^{III}(DPA)_3]^{3-}$ series.

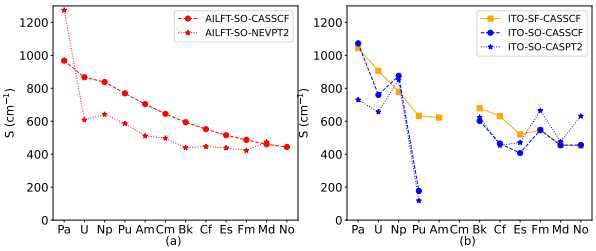

Figure 6: Crystal field total strength parameter S (in cm^{-1}) along the $[An^{III}(DPA)_3]^{3-}$ series. a: from AILFT, b: from ITO.

parameter. They are compared for the different methods in Fig. 6. The AILFT strength parameter deduced from SO-CASSCF smoothly decreases along the series following the overall decrease of the splitting of the $5f$orbitals (see Figure 5). With NEVPT2, the overall splitting increases slightly at the end of the series, leading to a small increase of the corresponding S. The ITO-CFPs, and the subsequent S parameter are deduced at SF-CASSCF, SO-CASSCF and SO-CASPT2 levels. The S deduces from AILFT probes the orbital level, SF-CASSCF includes the many-electron effects, SO-CASSCF the spin-orbit interactions, as the J-mixing and SO-CASPT2 the dynamical correlation. AILFT and SF-CASSCF are compared in Figure S7Crystal field total strength parameter S (in cm^{-1}) . a: from different methods along the $[An^{III}(DPA)_3]^{3-}$ series, b: for extrapolated and optimized geometries along the $[An^{III}(DPA)_3]^{3-}$ series, c: from AILFT (circles) and SF-CASSCF (squares) along the $[An^{III}(DPA)_3]^{3-}$ (red) and $[Ln^{III}(DPA)_3]^{3-}$ (blue) series. figure.caption.30c. The $[Ln^{III}(DPA)_3]^{3-}$ and $[An^{III}(DPA)_3]^{3-}$ series denote the same behavior, emphasized for the latter: in the first half of the series, S tends to be smaller with AILFT than with SF-CASSCF, and it is the reverse for the second half. The many-electron wave function depends on the filling of the f orbitals, the most energetic being the most antibonding. The effect of spin-orbit is analyzed by comparing the SF-CASSCF and SO-CASSCF (see Figure 6b) and the trends are jagged. The largest effect is obtained for the Pu(III) derivative, with a shrinking of the ground J manifold. This was already observed and discussed for the $La_{1-x}Pu_xPO_4$ crystal.[57] The J-mixing is around 2% in the lanthanides whereas it is increased by several order of magnitude in the actinides due the strong spin-orbit coupling, specially in the middle of the series (Pu, Bk, Cf, Es) where it reaches around 20-25%, as shown in Table 1. The effect of electron dynamic correlation on the ITO strength parameters (see Figure 6b) is relatively small, contrarily to AILFT (see Figure 6a).

S can be partitioned according to 2nd, 4th and 6th order contributions S^k (see Eq. S5Theoryequation.2.5) as shown in Fig. S6Dominant crystal field strength parameters (in cm^{-1}) of k^{th} order S^k and q^{th} index S_q along the $[An^{III}(DPA)_3]^{3-}$ series. figure.caption.29, which all are rotation invariant. The AILFT second order contribution S^2 is constant along the series, S^4 decreases slightly and S^6 decreases strongly. The same trends were found in the $[Ln^{III}(DPA)_3]^{3-}$ series, the decrease of the S^6 being more pronounced in the present case. S can be partitioned as well according to the index, S_q (see Eq. S7Theoryequation.2.7). S_q is not rotation invariant. Since the z axis is along the C_3 axis, the S_q of index 0, 3 and 6 (see Eq. S7Theoryequation.2.7) are preponderant, S_6 showing the strongest decrease along the series, much more pronounced than in the $[Ln^{III}(DPA)_3]^{3-}$ series.

$HDPA^-$ versus DPA^{2-} ligands

As already mentioned, the $[An^{III}(DPA)_3]^{3-}$ complexes are known for An = Pu and Am[15] and the $[An^{III}(HDPA)_3]$ complexes for An = Am, Cm, Bk and Cf.[16,17] The structures of $[Am(DPA)_3(C_3H_5N_2)_3]\cdot 3H_2O$ and $[An^{III}(HDPA)_3]\cdot nH_2O$ are very similar, showing that the protonation of the DPA^{2-} ligand does not impact the geometrical structure of the coordination sphere.

There are two different conformers in the $[An^{III}(HDPA)_3]\cdot nH_2O$ crystals, due to the hydrogen bond network between two DPA ligands of two different molecules. The position of the hydrogen atoms on the DPA ligands is not determined by the XRD and due to the hydrogen bonding network, it is expected to fluctuate. In Table S11SO-CASPT2 energies (in cm^{-1}) of the lowest states of the $[An(HDPA)_3]$ complexes depending on the XRD structure and the position of the H atom on the DPA ligand. cis: the 3 H are on the same side of the equatorial plane, trans; 2 H on one side, 1 H on the other side (see Figure S8The Δ cis (a) and trans (b) $[Bk^{III}(HDPA)_3]$ complexes. The protonated positions are highlighted with larger spheres for the H atoms. figure.caption.31).[2,17]

table.caption.20, we compare the electronic structure of the $[Bk^{III}(HDPA)_3]$ and $[Cf^{III}(HDPA)_3]$ complexes, for the two sites, each of them with two different positions of the protons, either on the same side of the equatorial plane, denoted cis, or two on one side and the other on the opposite side, denoted trans (see Figure S8The Δ cis (a) and trans (b) $[Bk^{III}(HDPA)_3]$ complexes. The protonated positions are highlighted with larger spheres for the H atoms. figure.caption.31). These two conformers can be considered representative of all other conformations. The position of the three protons impacts strongly the electronic structure. Namely, the protons are close to a coordinating oxygen atom, and consequently, impacts the crystal field. The effect is the most dramatic in the trans conformer, since in this case the ternary symmetry is broken.

The ab initio magnetic curves are compared to the experimental ones in Figures S9χT as a function of temperature for the $[Cf(HDPA)_3]$ (left) and $[Bk(HDPA)_3]$ (right) complexes, experimental[2,17] and from SO-CASPT2 for different structures (see Table S11SO-CASPT2 energies (in cm^{-1}) of the lowest states of the $[An(HDPA)_3]$ complexes depending on the XRD structure and the position of the H atom on the DPA ligand. cis: the 3 H are on the same side of the equatorial plane, trans; 2 H on one side, 1 H on the other side (see Figure S8The Δ cis (a) and trans (b) $[Bk^{III}(HDPA)_3]$ complexes. The protonated positions are highlighted with larger spheres for the H atoms. figure.caption.31).[2,17] table.caption.20). The data for the corresponding $[An^{III}(DPA)_3]^{3-}$ and $[Ln^{III}(DPA)_3]^{3-}$ (SO-CASSCF) are given for comparison. figure.caption.32 and S10Magnetization as a function of magnetic field at 1.8 K for the $[Cf(HDPA)_3]$ complex, experimental[2] and from SO-CASPT2 for different structures (see Table S11SO-CASPT2 energies (in cm^{-1}) of the lowest states of the $[An(HDPA)_3]$ complexes depending on the XRD structure and the position of the H atom on the DPA ligand. cis: the 3 H are on the same side of the equatorial plane, trans; 2 H on one side, 1 H on the other side (see Figure S8The Δ cis (a) and trans (b) $[Bk^{III}(HDPA)_3]$ complexes. The protonated positions are highlighted with larger spheres for the H atoms. figure.caption.31).[2,17] table.caption.20). The data for the corresponding $[An^{III}(DPA)_3]^{3-}$ and $[Ln^{III}(DPA)_3]^{3-}$ (SO-CASSCF) are given for comparison. figure.caption.33. Since the conformers differ by their low-lying state energies, the χT are much different at low temperature but all curves converge on the same high-temperature plateau. This plateau is slightly lower for the corresponding lanthanide, because the splitting of the ground J manifold is larger than room temperature thermal energy. The experimental curve should be compared to the average of the conformers: for the Bk complex, it suits well but for the experimental Cf curve lies above all calculated curves. The Cf complex is a Kramers ion, the magnetization depends on the g factors of the ground Kramers doublet: they are almost the same for all Cf conformers, and smaller than for the Dy complex.

Comparison with the $[Ln^{III}(DPA)_3]^{3-}$ and $[An^{IV}(DPA)_3]^{2-}$ series

In this Section, we compare the available data for the $[Ln^{III}(DPA)_3]^{3-}$, $[An^{III}(DPA)_3]^{3-}$ and $[An^{IV}(DPA)_3]^{2-}$ series. We have previously seen that the bond distances in the coordination sphere were similar in terms of ionic radius for the Ln(III) and An(III) complexes, but that for the An(IV) complexes, the bonding with the nitrogen atoms was longer, leading to a deformation of the DPA ligand.

The CFPs in crystal-field theory arise solely from the charge and position of the ligands and from the charge of the metal. In the modeling of the dipolar contribution to chemical shift of pNMR in lanthanides, the B_0^2 is considered to be constant along the series.[58] This hypothesis is clearly not verified in the present case as can be seen by the comparison of the crystal field strength parameter S for the three series in Figures 7a at the orbital level, S decreases for the three series. In the case of Ln(III) complexes, it has been shown that within a point charge model reproducing the electrostatic potential of the ligands, the CFPs are rather constant across the series, due a counterbalance between the shrinking of the coordination sphere and the greater compactness of the 4f orbitals.[22] The decrease in the series was attributed to covalent effects. S for the An(IV) is about 50% higher than for the An(III) and three times greater than for Ln(III). This follows the splitting of ground J manifold of 2000-4000 cm^{-1} for the An(IV), 500-1000 cm^{-1} for the An(III) and about 300 cm^{-1} for the Ln(III) complexes. Even not constant, the trends are smooth, following the picture of electrostatic and molecular orbital interaction of ligand-field theory.

The ITO CFPs in Figures 7b effectively incorporate the many-electron and spin-orbit interactions. The trend in the Ln(III) series remains the same what suggests that the CFPs are not affected by many-electron interactions and spin-orbit coupling The trend is more irregular for the two actinide series, due to the effect of the J-mixing. In the two actinide series, covalent effects are larger and the electrostatic interaction larger for the An(IV) series leading to larger values of S. At the orbital level, S^2 is rather constant in a given series, larger and identical for the An(III) and An(IV) series. The largest contributions and the most variable ones are the 4th and 6th order ones, S^4 and S^6. They are much larger for actinides, larger for An(IV) than for An(III) (see

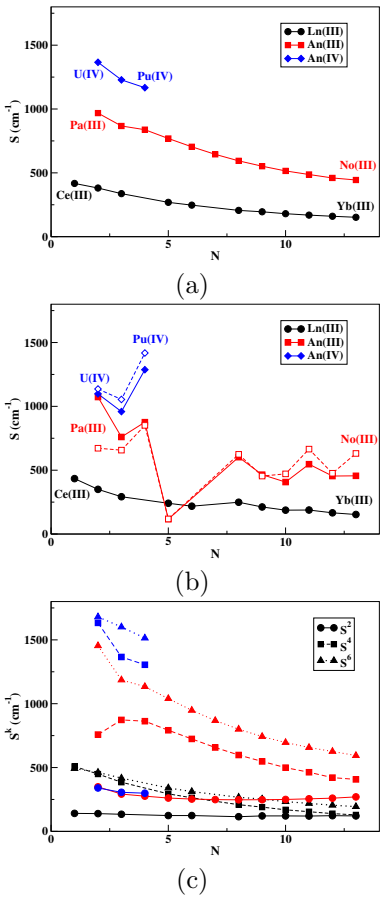

Figure 7: Crystal field strength parameter S (in cm^{-1}) for the $[Ln^{III}(DPA)_3]^{3-}$ (black, from[22]), $[An^{III}(DPA)_3]^{3-}$ (red, this work) and $[An^{IV}(DPA)_3]^{2-}$ (blue, from[23]) series; a: at the orbital level (AILFT), b: at SO-CASSCF (plain) and SO-CASPT2 (dashed) levels (ITO), c: S^k AILFT.

Figure 7). It suggests that the 4th and 6th orders are much more affected by covalent effects than the 2nd order.

The magnetic properties of the three series are compiled in Tables S19Mean magnetic susceptibility χ_m (in 10^{-8} $m^3.mol^{-1}$) at 300 K for the $[Ln^{III}(DPA)_3]^{3-}$, $[An^{III}(DPA)_3]^{3-}$ and $[An^{IV}(DPA)_3]^{2-}$ series, calculated and experimental. table.caption.34 and S20Axial magnetic susceptibility $\Delta\chi_{ax}$ (in 10^{-8} $m^3.mol^{-1}$) at 300 K for the $[Ln^{III}(DPA)_3]^{3-}$, $[An^{III}(DPA)_3]^{3-}$ and $[An^{IV}(DPA)_3]^{2-}$ series, calculated and experimental. table.caption.35 and shown in Figures 8. The mean magnetic susceptibility χ_m was probed using SQUID and pNMR with Evans method.[60] It shows the well known double-bell shaped curve following the $g_J J(J+1)$ saturation value for the χT (see Table S3Ground L and J of the free ions. g_J is the Landé g-factor, μ^J_{eff} is the effective magnetic moment (in μ_B) and χ^J_m is the Curie magnetic susceptibility (in 10^{-8} $m^3 mol^{-1}$). table.caption.5). As already reported for aqueous complexes,[61–63] while the value at 300 K is close to the saturation value

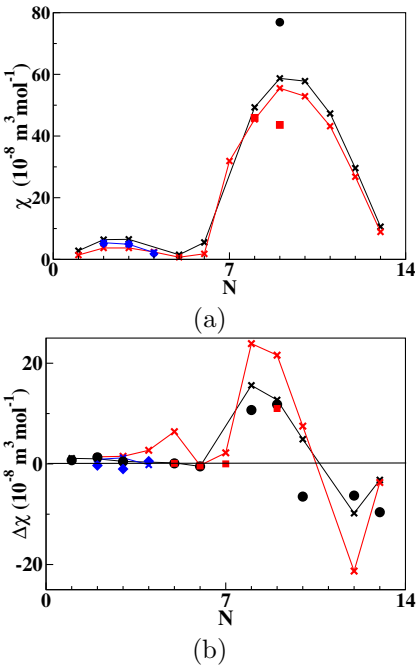

Figure 8: Mean (a) and axial (b) magnetic susceptibility (χ_m and $\Delta\chi_{ax}$ in 10^{-8} $m^3.mol^{-1}$) at 300 K for the $[Ln^{III}(DPA)_3]^{3-}$ (black, from[15–17]), $[An^{III}(DPA)_3]^{3-}$ (red) and $[An^{IV}(DPA)_3]^{2-}$ (blue, from[59]) series, calculated (crosses) and experimental (icons) (see Tables S19Mean magnetic susceptibility χ_m (in 10^{-8} $m^3.mol^{-1}$) at 300 K for the $[Ln^{III}(DPA)_3]^{3-}$, $[An^{III}(DPA)_3]^{3-}$ and $[An^{IV}(DPA)_3]^{2-}$ series, calculated and experimental. table.caption.34 and S20Axial magnetic susceptibility $\Delta\chi_{ax}$ (in 10^{-8} $m^3.mol^{-1}$) at 300 K for the $[Ln^{III}(DPA)_3]^{3-}$, $[An^{III}(DPA)_3]^{3-}$ and $[An^{IV}(DPA)_3]^{2-}$ series, calculated and experimental. table.caption.35).

for Ln(III) complexes, $\chi_m T$ is smaller for the actinide derivatives due to the larger splitting of the ground J manifold, larger than the thermal energy at room temperature, and the plateau is not fully reached at room temperature.

The axial anisotropy $\Delta\chi_{ax}$ of the χ tensor can be deduced from pNMR measurements. This needs the separation of the contact and dipolar contributions to the paramagnetic chemical shifts. Assuming an axial symmetry, the dipolar term is related to $\Delta\chi_{ax}$ and the separation is obtained from the temperature dependence of the shifts. As shown by Bleaney,[58,64] at the saturation of the ground J manifold, the $\Delta\chi_{ax}$ behaves as $-C_J\alpha_J^{(2)}B_0^2T^{-2}$ where $\alpha_J^{(2)}$ is the reduced matrix element of second order (see Eq. S3Theoryequation.2.3) and C_J is Bleaney constant, expressed in terms of g_J and J. In the three series, B_0^2 is positive, corresponding to a prolate coordination sphere, B_0^2 being related to the quadrupole moment of the ligands.[65] The sign of $\alpha_J^{(2)}$ alternates in the series[66] following the filling of the f orbitals. It is positive for Pm-Sm and Er-Yb and negative for Ce-Nd and Tb-Ho. The sign of $\Delta\chi_{ax}$ in Table S19Mean magnetic susceptibility χ_m (in 10^{-8} $m^3.mol^{-1}$) at 300 K for the $[Ln^{III}(DPA)_3]^{3-}$, $[An^{III}(DPA)_3]^{3-}$ and $[An^{IV}(DPA)_3]^{2-}$ series, calculated and experimental. table.caption.34 follows this trend in the three series, both for the ab initio and experimental data: $\Delta\chi_{ax}$ is positive for $N=1-3;8-10$ and negative for $N=4-5;11-13$. Contrarily to χ_m, the values of $\Delta\chi_{ax}$ are larger for the actinides than for the corresponding lanthanide: the splitting of the ground J manifold being larger, at room temperature, this manifold is less uniformly populated and this leads to a larger anisotropy. The alternation of sign was observed in the Ln(III) series,[67] although the limitations to Bleaney theory.[68–71] It is recovered in the An(III) series, even if the 4th and 6th order crystal field terms are the largest.

The bond interaction was analyzed in the three series, using QTAIM (quantum theory of atoms-in-molecules).[14,23] In all cases, it was shown that the analysis of the electronic density including or not spin-orbit coupling leads to similar values; the spin-orbit coupling does not affect the bonding analysis since it mixes states with similar electronic densities.[72] The descriptors are represented against the M-L bond distance in Figure 9 for the three series. The four descriptors behave roughly linearly with the bond length, they do not depend on the nature of the coordinating atom (N or O) but on the central cation (Ln(III), An(III) or An(IV)). The bonding is mostly ionic, and the covalent contributions are slightly larger with the An(IV) cations, both for the An-O and An-N bonds. The descriptors for An(III) and Ln(III) complexes are close, slightly larger for the former, while they are much

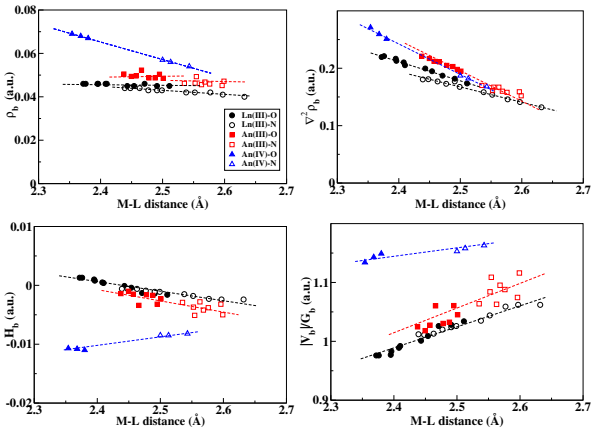

Figure 9: QTAIM descriptors ρ_b, $\nabla^2\rho_b$, H_b and $|V_b|/G_b$ at the BCPs for the M-O (filled icons) and M-N (empty icons) bonds in the $[Ln^{III}(DPA)_3]^{3-}$ (black, from[23]), $[An^{III}(DPA)_3]^{3-}$ (red, from[14]) and $[An^{IV}(DPA)_3]^{2-}$ (blue, from[23]) series. The dashed lines indicate the trends.

larger for the An(IV) series. The density at bond-critical points ρ_b is about 30 and 50 % larger for the An(IV)-N and An(IV)-O bonds than for the Ln(III) complexes, while it is only 10 % larger in the An(III) complexes. In all cases, the trends for the $[An^{III}(DPA)_3]^{3-}$ series are never more different by 10 % from the $[Ln^{III}(DPA)_3]^{3-}$. The trend of the $[An^{IV}(DPA)_3]^{2-}$ series differ much more, even qualitatively.

Conclusions

In this work, the CFPs were calculated in the $[An^{III}(DPA)_3]^{3-}$ series, completing previous works on the $[Ln^{III}(DPA)_3]^{3-}$ and $[An^{IV}(DPA)_3]^{2-}$ series. The overall splitting of the ground J manifold and as a consequence, the CFPs and crystal-field strength parameters were found intermediate between the Ln(III) and An(IV) complexes. They all decrease in the series, as for the other two series. The CFPs follow the ternary symmetry, with a predominance of indexes $q=0$, 3 and 6. The 4th and 6th orders are the prevailing ones and decrease strongly along the series.

For the Pa(III) complex, the deviation to the free ion is large, this gap still exists for U and Pu, and then is rather small from Bk. This can be gauged by two indicators: i) the distance between the model and ab initio magnetic moment matrices in the ground J manifold (see Table S13δL_u $(u=x,y,z)$ (in μ_B), δm_u $(u=x,y,z)$ (in μ_B) and δh (in cm^{-1}) distances between *ab initio* and model matrices (see Eqs. S8ITO and AILFT methodsequation.2.8 and S9ITO and AILFT methodsequation.2.9).table.caption.22) ii) the Slater-Condon parameters in the An(III) complex as compared to those of the free ion, quantified

by the nephelauxetic reduction factor (see Figure 4 and Table S12Slater–Condon (F^2, F^4 and F^6), SOC (ζ) parameters (in cm^{-1}) and nephelauxetic reduction factor α (in %) calculated with AILFT method for the $[An^{III}(DPA)_3]^{3-}$series. The free ion parameters are collected from Ref.[7] table.caption.21). The participation of the $6d$ to actinide spin population rapidly drops while the degree of spin delocalization drops at the beginning and slightly increases at the end of the series.

In many aspects, the An(III) series is closer to the Ln(III) one than to the An(IV): the structural parameters of the coordination sphere are similar in terms of ionic radius except for the An(IV)-N distance which is shorter, leading to a larger deformation of the DPA ligand in the An(IV) series. The QTAIM descriptors in the An(III) series represented in term of M-L bond distance differ by no more than 10 % from the Ln(III) series, whereas their behavior is much more different from the An(IV) series, both qualitatively and quantitatively.

The magnetic properties follow the same trends in the three series: the average magnetic susceptibility χ_m exhibits the double-bell shaped curve following the expected value of the effective moment μ_{eff}^J but the values are damped in the actinide complexes, since the splitting of the ground J manifold is larger than thermal energy. The axial anisotropy $\Delta\chi_{ax}$ follows qualitatively Bleaney theory, with three alternation of sign in the series, although this theory is based on only the axial CFP of 2nd order and it was shown that in actinide complexes, the 4th and 6th orders CFP prevail. The anisotropy is larger in actinides than in lanthanides, due to a lower population of excited states at room temperature. The low temperature magnetic properties are more unpredictable, as shown by the comparison between the HDPA and DPA ligands, and the sensibility to the location of the protonated position.

Supporting Information

Geometry of the complexes, Crystal Field Parameters (theory and results for the $[An^{III}(DPA)_3]^{3-}$ series), Ab initio results for the $[An^{III}(DPA)_3]^{3-}$ series, magnetic properties for the $[Cf(HDPA)_3]$ and $[Bk(HDPA)_3]$ complexes. (PDF)

Acknowledgments

This work was supported by the ANR under convention N°ANR-17-CE06-0010.

References

[1] Morss, L. R.; Edelstein, N. M.; Fuger, J.; Katz, J. J.; Morss, L. *The chemistry of the actinide and transactinide elements;* volume 1 Springer: The Netherlands, 2006.

[2] Neidig, M. L.; Clark, D. L.; Martin, R. L. Covalency in f-element complexes. *Coord. Chem. Rev.* **2013**, *257*, 394 – 406.

[3] Minasian, S. G.; Keith, J. M.; Batista, E. R.; Boland, K. S.; Clark, D. L.; Kozimor, S. A.; Martin, R. L.; Shuh, D. K.; Tyliszczak, T. New evidence for 5f covalency in actinocenes determined from carbon K-edge XAS and electronic structure theory. *Chem. Sci.* **2014**, *5*, 351–359.

[4] Magnani, N. Spectroscopic and magnetic investigations of actinide-based nanomagnets. *Int. J. Quantum Chem.* **2014**, *114*, 755–759.

[5] Magnani, N.; Colineau, E.; Griveau, J.-C.; Apostolidis, C.; Walter, O.; Caciuffo, R. A plutonium-based single-molecule magnet. *Chem. Commun.* **2014**, *50*, 8171–8173.

[6] Kelley, M. P.; Su, J.; Urban, M.; Luckey, M.; Batista, E. R.; Yang, P.; Shafer, J. C. On the origin of covalent bonding in heavy actinides. *J. Am. Chem. Soc.* **2017**, *139*, 9901–9908.

[7] Kaltsoyannis, N. Does covalency increase or decrease across the actinide series? Implications for minor actinide partitioning. *Inorg. Chem.* **2013**, *52*, 3407–3413.

[8] Chandrasekar, A.; Ghanty, T. K. Uncovering heavy actinide covalency: Implications for minor actinide partitioning. *Inorg. Chem.* **2019**, *58*, 3744–3753.

[9] Kloditz, R.; Fichter, S.; Kaufmann, S.; Brunner, T. S.; Kaden, P.; Patzschke, M.; Stumpf, T.; Roesky, P. W.; Schmidt, M.; März, J. Series of tetravalent actinide amidinates: Structure determination and bonding analysis. *Inorg. Chem.* **2020**, *59*, 15670–15680.

[10] Yu, X.; Sergentu, D.-C.; Feng, R.; Autschbach, J. Covalency of Trivalent Actinide Ions with Different Donor Ligands: Do Density Functional and Multiconfigurational Wavefunction Calculations Corroborate the Observed 'Breaks'?. *Inorg. Chem.* **2021**, *60*, 17744–17757.

[11] Carnall, W. T. A systematic analysis of the spectra of trivalent actinide chlorides in D3h site symmetry. *J. Chem. Phys.* **1992**, *96*, 8713–8726.

[12] Aravena, D.; Atanasov, M.; Neese, F. Periodic trends in lanthanide compounds through the eyes of multireference ab initio theory. *Inorg. Chem.* **2016**, *55*, 4457–4469.

[13] Jung, J.; Atanasov, M.; Neese, F. Ab Initio ligand-field theory analysis and covalency trends in actinide and lanthanide free ions and octahedral complexes. *Inorg. Chem.* **2017**, *56*, 8802–8816.

[14] Yu, X.; Sergentu, D.-C.; Feng, R.; Autschbach, J. Covalency of trivalent actinide ions with different donor ligands: Do density functional and multiconfigurational wavefunction calculations corroborate the observed "Breaks"?. *Inorg. Chem.* **2021**, *60*, 17744–17757.

[15] Autillo, M.; Guerin, L.; Dumas, T.; Grigoriev, M. S.; Fedoseev, A. M.; Cammeli, S.; Solari, P. L.; Guilbaud, P.; Moisy, P.; Bolvin, H.; Berthon, C. Insight of the metal-ligand interaction in f elements complexes by paramagnetic NMR spectroscopy. *Chem. Eur. J.* **2019**, *25*, 4435.

[16] Cary, S. K. *et al.* Emergence of californium as the second transitional element in the actinide series. *Nat. Commun.* **2015**, *6*, 1–8.

[17] Silver, M. A.; Cary, S. K.; Johnson, J. A.; Baumbach, R. E.; Arico, A. A.; Luckey, M.; Urban, M.; Wang, J. C.; Polinski, M. J.; Chemey, A.; Liu, G.; Chen, K.-W.; Cleve, S. M. V.; Marsh, M. L.; Eaton, T. M.; van de Burgt, L. J.; Gray, A. L.; Hobart, D. E.; Hanson, K.; Maron, L.; Gendron, F.; Autschbach, J.; Speldrich, M.; Kögerler, P.; Yang, P.;

Braley, J.; Schmitt, T. E. A. Characterization of berkelium(III) dipicolinate and borate compounds in solution and the solid state. *Science* **2016**, *353*, aaf3762.

[18] Desreux, J. F.; Reilley, C. N. Evaluation of Contact and Dipolar Contributions to ^{1}H and ^{13}C Paramagnetic NMR Shifts in Axially Symmetric Lanthanide Chelates.. *J. Am. Chem. Soc.* **1976**, *98*, 2105–2109.

[19] Rigault, S.; Piguet, C. Predictions and assignments of NMR spectra for strongly paramagnetic supramolecular Lanthanide complexes: The effect of the "Gadolinium break". *J. Am. Chem. Soc.* **2000**, *122*, 9304–9305.

[20] Ouali, N.; Bocquet, B.; Rigault, S.; Morgantini, P. Y.; Weber, J.; Piguet, C. Analysis of paramagnetic NMR spectra of triple-helical lanthanide complexes with 2,6-dipicolinic acid revisited: A new assignment of structural changes and crystal-field effects 25 years later. *Inorg. Chem.* **2002**, *41*, 1436–1445.

[21] Autillo, M.; Islam, M. A.; Héron, J.; Guérin, L.; Acher, E.; Tamain, C.; Illy, M.-C.; Moisy, P.; Colineau, E.; Griveau, J.-C.; Berthon, C.; Bolvin, H. Temperature dependence of ^{1}H paramagnetic chemical shifts in actinide complexes, beyond Bleaney's theory: The $An^{VI}O_2^{2+}$-dipicolinic acid complexes (An=Np, Pu) as an example. *Chem. Eur. J.* **2021**, *27*, 7138–7153.

[22] Jung, J.; Islam, M. A.; Pecoraro, V. L.; Mallah, T.; Berthon, C.; Bolvin, H. Derivation of lanthanide series crystal field parameters from first principles. *Chem. Eur. J.* **2019**, *25*, 15112–15122.

[23] Autillo, M.; Islam, M. A.; Jung, J.; Pilmé, J.; Galland, N.; Guerin, L.; Berthon, C.; Tamain, C.; Bolvin, H. Crystallographic structure and crystal field parameters in the $[An^{IV}(DPA)_3]^{2-}$ series, An = Th, U, Np, Pu.. *Phys. Chem. Chem. Phys.* **2020**, *22*, 14293–14308.

[24] Bolvin, H. Modeling Magnetic Properties of Actinide Complexes. In *Computational Modelling of Molecular Nanomagnets*, Vol. 34; Rajaraman, G., Ed.; Springer Nature Switzerland: , 2023.

[25] Neese, F. Software update: the ORCA program system, version 4.0. *Wiley Interdisciplinary Reviews: Computational Molecular Science* **2018**, *8*, e1327.

[26] Becke, A. Density-functional exchange-energy approximation with correct asymptotic behavior.. *Phys. Rev. A* **1988**, *38*, 3098.

[27] Grimme, S.; Ehrlich, S.; Goerigk, L. Effect of the damping function in dispersion corrected density functional theory. *J. Comput. Chem.* **2011**, *32*, 1456–1465.

[28] Pantazis, D. A.; Neese, F. All-electron scalar relativistic basis sets for the actinides. *J. Chem. Theory Comput.* **2011**, *7*, 677–684.

[29] Stoychev, G. L.; Auer, A. A.; Neese, F. Automatic generation of auxiliary basis sets. *J. Chem. Theory Comput.* **2017**, *13*, 554–562.

[30] Neese, F. An improvement of the resolution of the identity approximation for the formation of the Coulomb matrix. *J. Comput. Chem.* **2003**, *24*, 1740–1747.

[31] Reiher, M. Douglas-Kroll-Hess Theory: a relativistic electrons-only theory for chemistry. *Theor. Chem. Acc.* **2006**, *116*, 241–252.

[32] Nakajima, T.; Hirao, K. The Douglas-Kroll-Hess Approach. *Chem. Rev.* **2012**, *112*, 385–402.

[33] Neese, F. Efficient and accurate approximations to the molecular spin-orbit coupling operator and their use in molecular g-tensor calculations. *J. Chem. Phys.* **2005**, *122*, 034107.

[34] Angeli, C.; Cimiraglia, R.; Evangelisti, S.; Leininger, T.; Malrieu, J.-P. Introduction of n-electron valence states for multireference perturbation theory. *J. Chem. Phys.* **2001**, *114*, 10252–10264.

[35] Angeli, C.; Cimiraglia, R.; Malrieu, J.-P. N-electron valence state perturbation theory: a fast implementation of the strongly contracted variant. *Chem. Phys. Lett.* **2001**, *350*, 297–305.

[36] Angeli, C.; Cimiraglia, R.; Malrieu, J.-P. n-electron valence state perturbation theory: A spinless formulation and an efficient implementation of the strongly contracted and of the partially contracted variants. *J. Phys. Chem.* **2002**, *117*, 9138–9153.

[37] Aquilante, F. *et al.* Molcas 8: New capabilities for multiconfigurational quantum chemical calculations across the periodic table. *J. Comput. Chem.* **2016**, *37*, 506–541.

[38] Roos, B. O.; Taylor, P. R.; Siegbahn, P. E. A complete active space SCF method (CASSCF) using a density matrix formulated super-CI approach. *Chem. Phys.* **1980**, *48*, 157–173.

[39] Andersson, K.; Malmqvist, P. A.; Roos, B. O.; Sadlej, A. J.; Wolinski, K. Second-order perturbation theory with a CASSCF reference function. *J. Phys. Chem.* **1990**, *94*, 5483–5488.

[40] Peterson, K. A. Correlation consistent basis sets for actinides. I. The Th and U atoms. *J. Chem. Phys.* **2015**, *142*, 074105.

[41] Feng, R.; Peterson, K. A. Correlation consistent basis sets for actinides. II. The atoms Ac and Np-Lr. *J. Chem. Phys.* **2017**, *147*, 084108.

[42] Roos, B. O.; Lindh, R.; Malmqvist, P.-Å.; Veryazov, V.; Widmark, P.-O. Main group atoms and dimers studied with a new relativistic ANO basis set. *J. Phys. Chem. A* **2004**, *108*, 2851–2858.

[43] Douglas, M.; Kroll, N. M. Quantum electrodynamical corrections to the fine structure of helium. *Annals of Physics* **1974**, *82*, 89–155.

[44] Hess, B. A. Relativistic electronic-structure calculations employing a two-component no-pair formalism with external-field projection operators. *Phys. Rev. A* **1986**, *33*, 3742.

[45] Malmqvist, P. Å.; Roos, B. O.; Schimmelpfennig, B. The restricted active space (RAS) state interaction approach with spin–orbit coupling. *Chem. Phys. Lett.* **2002**, *357*, 230–240.

[46] Hess, B. A.; Marian, C. M.; Wahlgren, U.; Gropen, O. A mean-field spin-orbit method applicable to correlated wavefunctions. *Chem. Phys. Lett.* **1996**, *251*, 365.

[47] Bolvin, H. An Alternative Approach to the g-Matrix: Theory and Applications. *ChemPhysChem* **2006**, *7*, 1575–1589.

[48] White, F. D.; Dan, D.; Albrecht-Schmitt, T. E. Contemporary Chemistry of Berkelium and Californium. *Chem. Eur. J.* **2019**, *25*, 10251–10261.

[49] David, F. H.; Vokhmin, V. Thermodynamic properties of some tri- and tetravalent actinide aquo ions. *New J. Chem.* **2003**, *27*, 1627–1632.

[50] Shannon, R. D. Revised effective ionic radii and systematic studies of interatomic distances in halides and chalcogenides. *Acta Cryst.* **1976**, *A32*, 751–767.

[51] D'Angelo, P.; Zitolo, A.; Migliorati, V.; Chillemi, G.; Duvail, M.; Vitorge, P.; Abadie, S.; Spezia, R. Revised Ionic Radii of Lanthanoid(III) Ions in Aqueous Solution. *Inorg. Chem.* **2011**, *50*, 4572–4579.

[52] Condon, E. U.; Shortley, G. H. *The theory of atomic spectra;* Cambridge University Press: , 1963.

[53] Dieke, G. H. *Spectra and energy levels of rare earth ions in crystals;* John Wiley and sons: New-York, 1968.

[54] Atanasov, M.; Zadrozny, J. M.; Long, J. R.; Neese, F. A theoretical analysis of chemical bonding, vibronic coupling, and magnetic anisotropy in linear iron (II) complexes with single-molecule magnet behavior. *Chem. Sci.* **2013**, *4*, 139–156.

[55] Atanasov, M.; Daul, C.; Rauzy, C. New insights into the effects of covalency on the ligand field parameters: a DFT study. *Chem. Phys. Lett.* **2003**, *367*, 737–746.

[56] Ungur, L.; Chibotaru, L. F. Ab initio crystal field for lanthanides. *Chem.Eur. J.* **2017**, *23*, 3708–3718.

[57] Martel, L.; Islam, M. A.; Popa, K.; Vigier, J.-F.; Colineau, E.; Bolvin, H.; Griveau, J.-C. Local structure and magnetism of $La_{1-x}M_xPO4$ (M = Sm, ^{239}Pu, ^{241}Am) explained by experimental and computational analyses. *J. Phys. Chem. C* **2021**, *125*, 22163–22174.

[58] Bleaney, B. Nuclear magnetic resonance shifts in solution due to lanthanide ions. *J. Magn. Reson.* **1972**, *8*, 91–100.

[59] Islam, M. A.; Autillo, M.; Guérin, L.; Tamain, C.; Moisy, P.; Bolvin, H.; Berthon, C. Dipolar and contact paramagnetic NMR chemical shifts in An(IV) complexes with dipicolinic acid derivatives. *Inorg. Chem.* **2022**, *61*, 10329–10341.

[60] Evans, D. The determination of the paramagnetic susceptibility of substances in solution by Nuclear Magnetic Resonance. *J. Chem. Soc.* **1959**, 2003–2005.

[61] Wall, T. F.; Steve, J.; Autillo, M.; Nash, L. K.; Guerin, L.; Le Naour, C.; Moisy, P.; Berthon, C. Paramagnetism of aqueous actinide cations. Part I: Perchloric acid media. *Inorg. Chem.* **2014**, *53*, 2450–2459.

[62] Autillo, M.; Guerin, L.; Bolvin, H.; Moisy, P.; Berthon, C. Magnetic susceptibility of actinide(III) cations: Experimental and theoretical study. *Phys. Chem. Chem. Phys.* **2016**, *18*, 6515.

[63] Autillo, M.; Guerin, L.; Guillaumont, D.; Moisy, P.; Bolvin, H.; Berthon, C. Paramagnetism of aqueous actinide cations. Part II: Theoretical aspects and new measurements on An(IV). *Inorg. Chem.* **2016**, *55*, 12149–12157.

[64] Bleaney, B.; Dobson, M.; Levine, B. A.; Martin, R. B.; Williams, R. J. P.; Xavier, A. V. Origin of lanthanide nuclear magnetic resonance shifts and their uses. *J. Chem. Soc. Chem. Comm.* **1972**, *13*, 791–793.

[65] Rinehart, J. D.; Long, J. R. Exploiting single-ion anisotropy in the design of f-element single-molecule magnets. *Chem. Sci.* **2011**, 2078–2085.

[66] Abragam, A.; Bleaney, B. *Electronic paramagnetic resonance of transition ions;* Clarendon Press: Oxford, 1970.

[67] William Dew. Horrocks, J.; James P. Sipe, I. Lanthanide complexes as nuclear magnetic resonance structural probes: Paramagnetic anisotropy of shift reagent adducts. *Science* **1972**, *177*, 994–996.

[68] Funk, A. M.; Finney, K.-L. N. A.; Harvey, P.; Kenwright, A. M.; Neil, E. R.; Rogers, N. J.; Kanthi Senanayake, P.; Parker, D. Critical analysis of the limitations of Bleaney's theory of magnetic anisotropy in paramagnetic lanthanide coordination complexes. *Chem. Sci.* **2015**, *6*, 1655–1662.

[69] Blackburn, O. A.; Edkins, R. M.; Faulkner, S.; Kenwright, A. M.; Parker, D.; Rogers, N. J.; Shuvaev, S. Electromagnetic susceptibility anisotropy and its importance for paramagnetic NMR and optical spectroscopy in lanthanide coordination chemistry. *Dalton Trans.* **2016**, *45*, 6782–6800.

[70] Suturina, E. A.; Mason, K.; Geraldes, C. F. G. C.; Kuprov, I.; Parker, D. Beyond Bleaney's theory: experimental and theoretical analysis of periodic trends in lanthanide-induced chemical shift. *Angew. Chem. Int. Ed.* **2017**, *56*, 12215–12218.

[71] Vonci, M.; Mason, K.; Suturina, E. A.; Frawley, A. T.; Worswick, S. G.; Kuprov, I.; Parker, D.; McInnes, E. J. L.; Chilton, N. F. Rationalization of Anomalous Pseudocontact Shifts and Their Solvent Dependence in a Series of C3-Symmetric Lanthanide Complexes. *J. Am. Chem. Soc.* **2017**, *139*, 14166–14172.

[72] Alessandri, R.; Zulfikri, H.; Autschbach, J.; Bolvin, H. Crystal field in rare-earth complexes: from electrostatics to bonding. *Chem. Eur. J.* **2018**, *24*, 5538–5550.

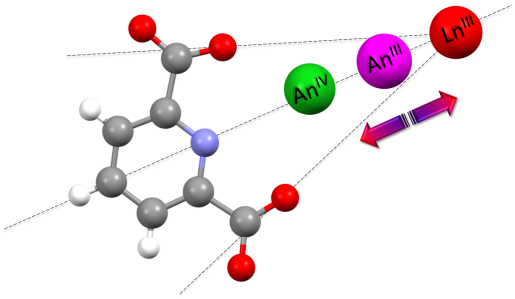

Comparison between the $[An^{III}(DPA)_3]^{3-}$, $[An^{IV}(DPA)_3]^{2-}$ and $[Ln^{III}(DPA)_3]^{3-}$ series: geometrical structure, crystal field parameters, magnetism